Mobile evaporite enhances the cycle of physical−chemical erosion in badlands

Ci-Jian Yang[1, 2], Pei-Hao Chen[1], Erica D. Erlanger[2], Jens M. Turowski[2], Sen Xu[2], Tse-Yang Teng[3], Jiun-Chuan Lin[1], Jr-Chuang Huang[1]

1. Department of Geography, National Taiwan University, No. 1, Sec. 4, Roosevelt Rd., Taipei 10617, Taiwan.

2. German Research Centre for Geosciences (GFZ), Telegrafenberg 14473, Potsdam, Germany.

3. Sustain-vision Consulting Co. Ltd., Taipei 11168, Taiwan.

Correspondence to: Ci-Jian Yang (d03228001@ntu.edu.tw)

Abstract. Chemical weathering driven by physical erosion is ~~one~~ a ~~of the manifestations of~~ natural process~~es~~ that strongly affect s chemical and solid matter budgets at the Earth's surface. However, the influence of extreme climatic erosion on chemical weathering dynamics is poorly understood. Badland landscapes formed in highly erodible, homogeneous substrates have the potential to respond to individual events on scales that are rapid enough for direct observation. Here, we assess the geochemical and grain-size composition of suspended sediment and riverine chemistry measurements collected from two catchments during the 2017 Nesat and Haitang typhoons in southwestern Taiwan. During the typhoons, the ~~sodium adsorption ratio~~Na^+ concentration covaried with suspended sediment concentration, which we attributed to sodium-induced deflocculation. Evaporite weathering at peak rainfall is succeeded by peak silicate weather ing at maximum discharge, which dominates the weathering signal of the event. Overall, our observations suggest that initial weathering of near-surface evaporite enhances the physical erosion of silicate rock during extreme rainfall events.

1. Introduction

Chemical weathering induced by physical erosion controls nutrient supply to ecosystems (Milligan and Morel, 2002), reflects dynamic surface processes (e.g., Calmels et. al., 2011; Clift et. al., 2014; Emberson et. al., 2016; Meyer et. al., 2017), and regulates the global carbon cycle and the evolution of Earth's long-term climate (Berner et al., 1983; Ram et al., 1992; Gaillardet et al., 1999). In most landscapes, physical erosion and chemical weathering operate on geological timescales that may be difficult to observe on human timescales (e.g., Maher et al., 2014). However, in many landscapes ~~studies show that most~~ erosion dominantly occurs during stochastic events, such as storms (e.g., Hartshorn et al., 2002; Lee et al., 2020; Wang et al., 2021). In particular, typhoons are able to transport large volumes of water and dissolved solids within hours to days, allowing us to observe the interactions between physical erosion and chemical weathering in landscapes impacted by them. Nevertheless, observations of the interaction between extreme physical erosion and chemical weathering dynamics are limited (Meyer et. al., 2017). Furthermore, the ~~Lack~~ lack of high-frequency stream water sampling leads to a fundamental difficulty in constraining the dynamic behavior between physical erosion and chemical weathering during a high discharge period (e.g., a typhoon), which could have key implications for our ability to quantify topographic responses to these events. ~~the quantification of topographic responses.~~

Badlands are landscapes characterized by highly erodible and weathered substrates, ~~which~~ that are largely devoid of vegetation. The high erodibility of these landscapes provides a unique opportunity to investigate and quantify denudation processes that operate at short timescales (Cheng et al., 2019; Yang et al, 2019, 2021a; 2021b). Badlands is typically dominated by mudstones and clays, and ~~Soils~~ soils that contain clays saturated in sodium ions are particularly vulnerable to erosion by water. Sodium ions alter the layer charge of double-layered clay minerals (i.e. smectite) and cause the clays to deflocculate, which refers to the process of breaking up the clay (and ultimately the soil) into finer particles that are more easily washed away by water (e.g., Faulkner et al., 2004; Mitchell et al., 1993;

48 Rengasamy and Olsson, 1991; Rengasamy et al.,1984; Sherard et al., 1976; Kašanin-Grubin et. al.,

49 2018). Additionally, mineral assemblage affects the stability of soil aggregates; for example, small

50 amounts of smectite in kaolinitic materials cause it to be more dispersive and unstable (Levy et al.,

51 1993).

52

53 Previous studies in the badlands of southwestern (SW)~~SW~~ Taiwan have revealed that ~~dissolving~~ halite

54 and gypsum dissolve at depth and migrate to the hillslope surface and deposit in desiccation cracks

55 during the dry season (Higuchi et al., 2013, 2015; Nakata and Chigira, 2009). Others have observed

56 that~~This produces~~ pore waters found in the near-surface mudstone have ~~with a concentration of~~ Na$^+$

57 concentrations of 1−3 million μmol/L at 1−2 cm depth (Nakata and Chigira, 2009). Mud cracks lead

58 to the properties of the mudstone, e.g., rock density, water permeability, and ion concentration between

59 the surface (a few centimeters to 10 cm depth) and bedrock are different (Fig. S1). For example, the

60 bedrock hardly participates in physical erosion during a rainfall event due to low permeability. We

61 hypothesize that the dissolved~~dissolving~~ halite and gypsum re-crystallizes in the near-surface and ~~is~~

62 are deposited in the mudstone cracks through capillary action during the dry season. Subsequent

63 ~~extreme~~ precipitation dissolves the evaporite, and the dissolved Na$^+$~~which~~ enhances erosion by clay

64 dispersity and ~~further~~ exposes more weatherable materials, forming a positive feedback cycle.

65 Assuming a mudstone substrate that is primarily comprised of silicate minerals, we expect that ~~the~~

66 concentration of ~~the~~ evaporite ions should be consistent with ~~the~~ changes in the sediment concentration

67 and the concentration of silicate ions.

68

69 To investigate this potential feedback~~the relationship~~ between evaporite dissolution and erosion, we

70 use suspended sediment concentrations (SSC) and stream chemistry data from two catchments in the

71 badlands of SW Taiwan (Fig. 1), collected at ~~collected with~~ a temporal resolution of 3 hours over 3

72 days. We interpret our observations in the badlands to reflect how the excess sodium that re-precipitates

73 at surface in dry season enhances physical erosion and chemical weathering in the following ~~during a~~

74 typhoon event. ~~, and the importance of this process for exposing fresh bedrock available for weathering~~

75 ~~in the following dry season.~~

76

77 **2. Geological and Meteorological Setting**

78 In Taiwan's badlands, the annual precipitation ~~exceeds~~ is about 2 m, and 90% of the rainfall is

79 concentrated in the rainy season. The rainy season lasts from May to October and reaches its peak in

80 August, with over 400 mm of precipitation within a single month. In contrast, less than 40 mm of

81 average monthly rainfall is measured from November to April. We collected river water samples from

82 two sites downstream of the studied badland areas. The first site, Nanxiong Bridge (NX), is located at

83 the midstream of the Erren River and has a drainage area of 175 km^2. This area includes badlands

84 covering an area of 4.37 km^2, which accounts for 2.49% of the total catchment area (Fig.1). The Erren

85 River catchment is predominantly underlain by Plio-Pleistocene mudstones, which are several

86 kilometers thick, and mainly feature illite (30.54%) and chlorite (28.70%) minerals (Tsai, 1984a).

87 During the dry seasons, the pore water chemistry in the near-surface mudstones is mainly composed

88 of Na^+, Cl^-, Ca^{2+} and SO_4^{2-} (Nakata and Chigira, 2009).

89

90 The gauging station at Nanxiong Bridge (NX) provides hourly discharge data for calculating sediment

91 and solute fluxes. The annual average discharge of Nanxiong Bridge station is 10.2 m^3/s, and the

92 typhoon season accounts for 84% of the total discharge. The meteorological station at Gutingkeng

93 (GTK) is located 5.5 km from Nanxiong Bridge and provides hourly precipitation data. Our second

94 sampling site is Guting (GT) Bridge, with an upstream drainage area of 79 km^2 and a badlands area of

95 1.87 km^2, corresponding to 2.37% of the total area. Guting Bridge is located adjacent to a badlands

96 conservation area, so the riverine water chemistry reflects the weathering products derived from the

97 adjacent hillslopes. Due to a lack of stream discharge observations at Guting Bridge, we use hourly

98 precipitation data at GTK, which is less than 1 km from the sampling site, to quantify the impact of

99 the typhoon events.

100
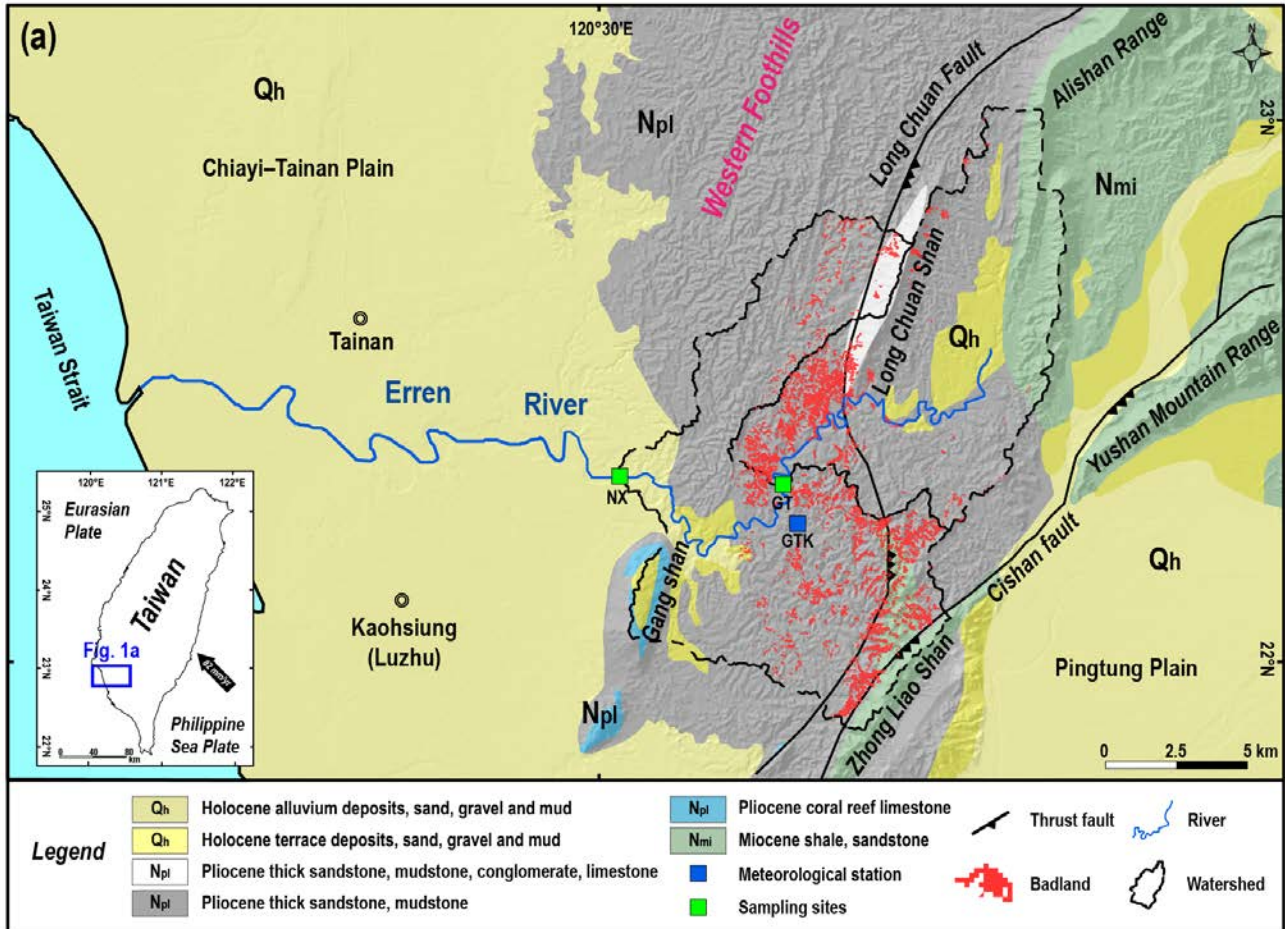
Figure 1. Location of sampling sites and geology of the study area. (a) The geological map of the study area (Source: Central Geological Survey, 2013). The green squares are sampling sites; hourly stream discharge data were obtained from the Nanxiong Bridge (NX) hydrometric station (Water Resources Agency). The blue square is the meteorological station, which provides hourly precipitation data (Central Weather Bureau, https://dbar.pccu.edu.tw/).

3. Methods and Materials

3.1 Water Sampling

We collected 42 stream samples from the two sampling sites for the typhoon period of July 2017. During sample collection, two 1000 ml PE bottles were dropped 1 to 2 meters below the water surface of the river simultaneously. Suspended sediment concentration (SSC) was subsequently calculated from the water collected in one of the PE bottles, and riverine chemistry was determined from water collected in the other bottle. Samples were filtered *in situ*, and the filtrate was preserved in the refrigerator for laboratory analysis. Additionally, 31 samples were collected from September 2014 to

116   December 2016 in the second half of every month at Nanxiong Bridge for non-typhoon periods, using

117   the same sampling procedure.

118

119   3.2 Dissolved load and sediment chemistry analysis

120   For the riverine dissolved load, we measured major dissolved anions (Cl^-, SO_4^{2-}, NO^{2-}, NO^{3-}, F^-) on an

121   Ion chromatography (IC, Metrohm Basic-883 plus), and we measured major dissolved cations (Na^+,

122   K^+, Mg^{2+}, Sr^{2+}, Ba^{2+}, Si^{4+}) on an ICP-OES (PerkinElmer, Optima 2100DV). We measured bulk

123   sediment chemistry from two samples of suspended sediment collected from Guting Bridge at low

124   flow before the typhoon event (2.26 m^3/s) and at the peak of runoff (724.32 m^3/s). About 0.7 g of dried

125   sediment sample was combusted in the muffle furnace at 650°C for 2 hours and then weighed to obtain

126   the loss on ignition (LOI). Afterwards, an aliquot of ~100 mg from the residue was digested with a

127   mixture of concentrated HF and aqua regia. After digestion and drying, the sample was dissolved in

128   0.3 N HNO_3 for elemental determination. Major elemental concentrations of sediment samples were

129   obtained by ICP-OES (Varian 720-ES) at the GFZ German Research Centre for Geosciences.

130

131   **3.3 Grain size of suspended load**

132   Before measuring grain size, we removed the non-clastic deposition, i.e., sea salt, organic matter, and

133   carbonate. To remove sea salt, ~1 g of dried sediment sample was added to 15 ml of distilled water,

134   placed in a shaker, and shaken at a speed of 4000 rpm for 5 minutes. The centrifuged supernatant was

135   then poured out and these steps were repeated 3 times. To remove organic matter, 10 ml of a 15%

136   H_2O_2 solution was added to the sediment and placed in an ultrasonic oscillator for 24 hours. After

137   adding a second 10 ml of H_2O_2 (15%) to confirm the completion of the reaction, the mixture was

138   centrifuged and the supernatant containing the organic matter was removed. The sediment was then

139   washed by adding 30 ml of distilled water, and the supernatant was again removed after centrifugation.

140   This washing step was repeated 3 times to remove residual H_2O_2 in the centrifuge tube. To remove the

carbonates, we added 10 ml of 10% HCl solution to the centrifuge tube and allowed the acid to react with the sediments for 24 hours. An additional 10 ml of HCl was then added to confirm the completeness of the reaction. The sample was then centrifuged, and the supernatant was decanted to remove the carbonates. The sample was then rinsed with 30 ml of distilled water, centrifuged, and decanted. This step was performed 3 times to remove any residual HCl.

To disperse sediment agglomeration, we added 10 ml of 1% $Na(PO_3)_6$ solution to the sediment and let the sample react for more than half a day. The grain size of the sediment samples was obtained by Laser Diffraction Particle Size Analyzer LA950 at the GFZ German Research Centre for Geosciences. By using LA950, we measured grains in the size range of between 100 nm to about 3 cm.

3.4 Calculation of the enriched ratio and sodium adsorption ratio (SAR)

In order to classify the supply of different ion sources during the typhoon event, we used the enriched ratio of concentration as a reference. The enriched ratio is the ion concentration at a certain time divided by the ion concentration at the first observation. A value greater than 1 represents a point in time when the sample is more concentrated relative to the first observation, whereas a value smaller than 1 represents a point in time when the sample is more diluted relative to the first observation. The first observation was sampled 6 hours before the typhoon which represents the background value of river water chemistry in this study.

Dissolved calcium and magnesium can stabilize soil aggregates and therefore facilitate enhance water permeability (Nadler et al., 1996). By contrast, excess sodium can disperse soil particles through deflocculation, thereby reducing water permeability (Hanson et al., 1999). The potential for material dispersion in badlands is generally determined by measuring the presence and behavior of sodium and is quantified by the sodium absorption ratio (SAR), (1):

$$SAR = \frac{Na^+}{\sqrt{\left(\frac{Ca^{2+}+Mg^{2+}}{2}\right)}} \tag{1}$$

Here, the cation measurements are expressed in milliequivalents per liter (meq/L). For pore water, ~~When~~ when SAR is greater than 13, the excess sodium causes soil particles to repel each other, preventing the formation of soil aggregates (Seelig, 2000; Horneck et al., 2007). Given the influence of soil structure, SAR value for irrigation water smaller than 3 is low, from 3 to 9 is medium and above 9 is high (Ayers and Westcot, 1985).

3.5 Calculation of TDS and chemical weathering rate

Riverine TDS is widely used to estimate chemical weathering rates of river catchments (e.g. Gaillardet et al. 1999). In this study, riverine TDS (in units of μmol/L) is expressed as:

$$TDS = TDS_{rain} + TDS_{evaporite} + TDS_{sil} + TDS_{carb} \tag{2}$$

where the contributions from precipitation (TDS_{rain}), evaporite ($TDS_{evaporite}$), silicate weathering (TDS_{sil}) and carbonate weathering (TDS_{carb}) are considered. We calculated the proportions of ion contributions from rainwater, evaporite, silicate and carbonate for Ca, Mg, Na, Cl, and SO$_4$ with the MEANDIR inversion model (Kemeny and Torres, 2021), a MATLAB script for inverting fractional contributions of end-members, and for constraining the chemical compositions of those end-members with Monte Carlo propagation of uncertainty. To exclude the input of precipitation (TDS_{rain}) from riverine TDS, we used local rainwater Cl^- concentrations with an average value of 68 μmol/L (Lu, 2014), and also the ratios of ~~Cl$^-$ and~~ SO_4/Cl^{2-}, Na/Cl^+, K/Cl^+, Mg/Cl^{2+}, Ca/Cl^{2+} in rainfall based on the rainfall chemistry from 2007 to 2013 reported by Lu (2014) (Table 1~~SO$_4^{2-}$/Cl$^-$ = 0.35, Na$^+$/Cl$^-$ =0.90, K$^+$/Cl$^-$ = 0.09, Mg^{2+}/Cl$^-$ = 0.18, Ca^{2+}/Cl$^-$ = 0.35~~) (Lu, 2014). ~~Thus, we estimated the annual deposition of those cations using equation (3):~~

$$[X]_{norain} = [X]_{river} - [X]_{rain} \tag{3}$$

$$TDS_{rain} = \sum[X]_{rain} \tag{4}$$

190   Here $[X]_{norain}$ reflects the remaining concentration of ion X after the removal of atmospheric inputs;

191     $[X]_{river}$ is the concentration of ion X in river water, and $[X]_{rain}$ is the concentration of ion X from

192   atmospheric deposition. In the second step, we corrected for evaporite inputs ($TDS_{evaporite}$) using the

193   following equation:

194     $$[X]_{NSS} = [X]_{norain} - [X]_{evap} = [X]_{norain} - \left([Cl]_{norain} \times \left(\frac{X}{Cl}\right)_{evap}\right) \tag{5}$$

195     $$TDS_{evaporite} = \sum[X]_{evap} \tag{6}$$

196   where $[X]_{NSS}$ is the concentration of ion X after the removal of ions attributed to evaporites, $[X]_{evap}$.

197     $[X/Cl]_{evap}$ is the ratio of ion X and Cl by using the end-member molar ratios of evaporite reported by

198   Burke et al. (2018), of which K/Cl is referred to Chao et al., (2011) (Table 1)~~$SO_4^{2-}/Cl^- = 0.4$, Na^+/Cl^-~~

199   ~~$= 1$, $Mg^{2+}/Cl^- = 0.10$, $Ca^{2+}/Cl^- = 0.5$, Burke et al., 2018; $K^+/Cl^- = 0.026$, Chao et al., 2013~~). Then, after

200   the correction for evaporite, the chemical weathering budget can be divided into contributions by

201   silicate (TDS_{sil}) and carbonate weathering (TDS_{carb}), expressed as:

202     $$TDS_{sil} = [Na]_{sil} + [K]_{sil} + [Mg]_{sil} + [Ca]_{sil} + [SiO_2]_{sil} \tag{7}$$

203     $$TDS_{carb} = [Mg]_{carb} + [Ca]_{carb} + [HCO_3]_{carb} \tag{8}$$

204     $$[HCO_3]_{carb} = \frac{1}{2}([Mg]_{crab} + [Ca]_{crab}) \tag{9}$$

205   where $[Na]_{sil}$ and $[K]_{sil}$ are riverine $[Na]_{NSS}$ and $[K]_{NSS}$ concentrations, respectively. We used

206   endmember values for silicate- and carbonate-dominated rocks reported by Gaillardet et al. (1999~~,~~)

207   (Table 1). We agree that the use of global endmembers leads to a larger range of estimations, but is

208   still appropriate in discussing trends in weathering rates.~~which gave ratios of Ca/Na =0.35 and Mg/Na~~

209   ~~=0.24 for silicates, and Ca/Na = 50 and Mg/Na =10 for carbonates.~~

210   Considering the hydrological response, we use flow weighted method to calculate the flux of solute

211 (Huang et al., 2012), expressed as:

$$Flux_{(rain,\ evap,\ sil,\ carb)} = \left. \left(m \times \frac{\sum_{i=1}^{n} TDS_{(rain,\ evap,\ sil,\ carb)\ i}}{\sum_{i=1}^{n} Q_i} \times Q_t\right) \middle/ \text{catchment area} \right. \tag{10}$$

213 where m is the conversion factor for a specific unit (ton/km^2/yr). Q_i is the hourly discharge
214 corresponding to sampling time. Q_t is total discharge during the year or during the typhoon.

217 **Table 1** Input end-members for the mixing model.

End-member	SO$_4$/Cl	Na/ Cl	K/ Cl	Mg/Cl	Ca/Cl
Precipitation	0.35	0.90	0.09	0.18	0.35
Evaporites	0.6±0.6	1.0±0	0.026	0.1±0.08	0.5±0.5
	Ca/Na	Mg/Na			
Silicates	0.35±0.25	0.24±0.2			
Carbonates	60±30	30±15			

219 **4. Results**

220 **4.1 Geochemistry of river water and suspended sediment**

221 In 2017, the Nesat and Haitang typhoons brought 579 mm of rainfall over three days, with a maximum

222 intensity of 74 mm/hr. The discharge at Nanxiong Bridge demonstrated that the climatic co-response

223 has two pulses (Fig. 2). Since the time interval between the two typhoons was less than 6 hours, we

224 define the two typhoons as one typhoon event and distinguish between a first and second discharge

225 pulse. We quantify time relative to the onset of the typhoon (0 hr). The first pulse occurred from 8.5 to

226 32.5 hr, with a mean water discharge of 66.2 m^3/s. The second pulse that occurred from 32.5 to 62.5

227 hr had a 5.5 times higher mean discharge of 369.2 m^3/s. The maximum discharge (753.2 m^3/s) was

228 observed during the second pulse at 44.5 hr (July ~~31th~~31st, 2017, at 6:00 a.m.) (Fig. 2).

230 At Nanxiong Bridge, SSC has a statistically significant positive correlation with SAR ($\rho = 0.51$, p <

231 0.05). SSC has two peaks, one during each ~~during the both~~ pulse~~s~~, but SAR only shows a peak during

232 the first pulse. During the first pulse, SSC ranged from 10 to 33757 mg/L and SAR increased from

233 ~~8.2~~1.44 and to ~~17.7~~3.14. During the second pulse, SSC increased from 5445 to 16900 mg/L and SAR

234 ~~is steadily~~remained about ~~7.3~~1.44.

235 The median grain size (D$_{50}$) ranged from 3.9 to 8.2 μm, with an average value of 5.6 μm during the

236 second pulse, and exhibited a positive correlation with discharge ($\rho = 0.40$). At Guting Bridge, SSC

237 has a statistically significant positive correlation with SAR ($\rho = 0.69$, $p < 0.05$) during the survey. SSC

238 ranged from 164 to 19538 mg/L before the first pulse and ranged from 2857 to 35920 mg/L during the

239 second pulse, while SAR showed a mean of ~~8.2~~1.46 and two peaks with a value over ~~20~~4 during both

240 pulses. D$_{50}$ ranged from 3.6 to 8.8 μm, with an average value of 5.3 μm during the second pulse, (Fig.

241 2). In terms of sediment chemistry at Guting Bridge, major elements of the two selected sediment

242 samples show that calcium and sodium accounted for about 10% of the mass loss between the typhoon

243 event (5.5 hr of duration) and the peak of discharge (41.5 hr of duration) (Table. S4).
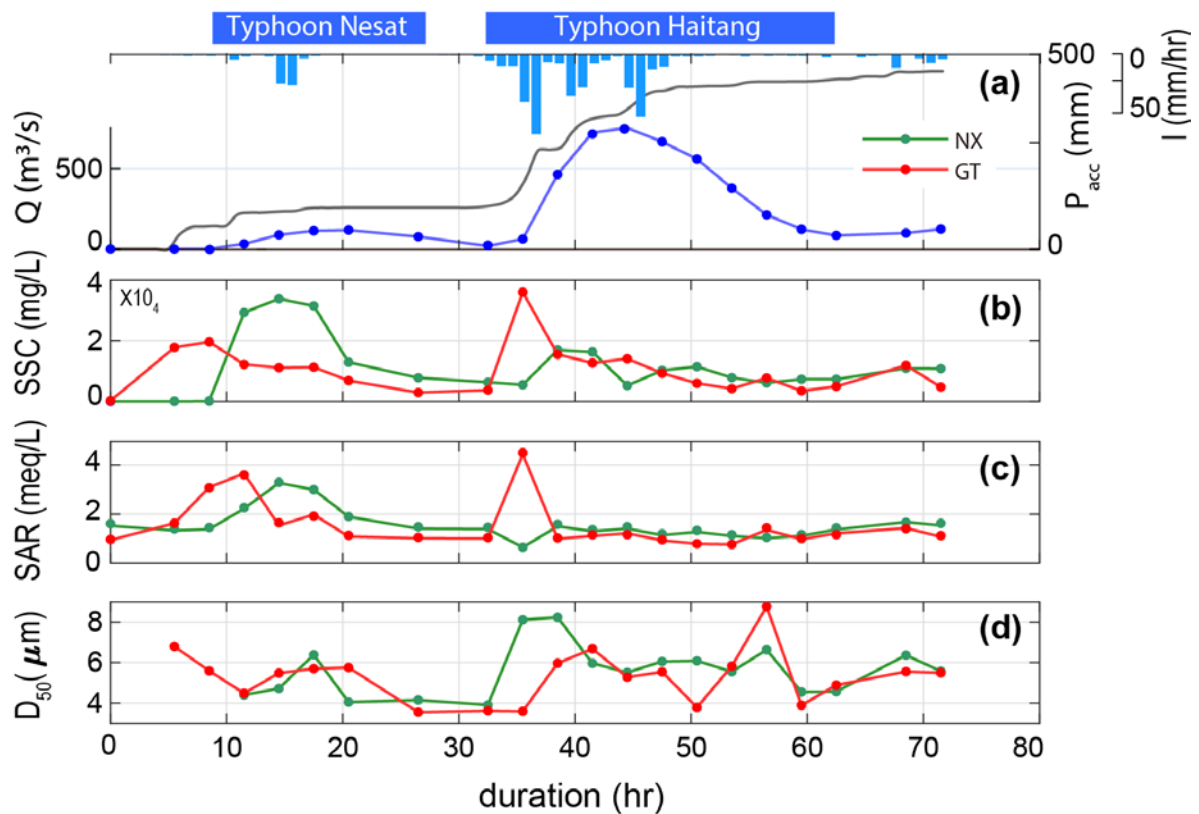
244

245 **Figure 2.** Timeseries SSC, SAR and median grain size of suspended sediment (D$_{50}$) at two sampling

246 sites. The blue line denotes hourly discharge (Q) at Nanxiong Bridge, and the blue bar denotes hourly

247 precipitation (I) at Gutingkeng station. The gray line denotes precipitation accumulation (P$_{acc}$), the

248 green line denotes the Nanxiong Bridge (NX) dataset, and the red line denotes the Guting Bridge (GT)

249 dataset.

250

The fractional proportions of TDS at Nanxiong Bridge during baseflow show that precipitation, evaporites, silicates, and carbonates contribute 3.0±1.1% (uncertainty gives the standard error of the mean), 28.7±14.6%, 26.9±6.5%, and 41.4±13.2%, respectively (Fig. 3a). During the typhoon event, the proportion of TDS at Nanxiong Bridge attributed to TDS_{rain} is 6.3±2.4%. $TDS_{evaporite}$ contributes 32.4±13.6% and increases from 27.4% to 61.1% at the incipient first pulse. TDS_{sil} contributes 39.5±15.2%, which is 12.6% higher than the non-typhoon period. TDS_{carb} contributes 21.8±11.5 % (Fig. 3b), which is 19.6% lower than the non-typhoon period. The fractional proportions of TDS at the Guting Bridge show that 6.5±2.1% of TDS is contributed by TDS_{rain}. $TDS_{evaporite}$ contributes 24.8±16.2% and increases from 13.6% to 61.6% at the incipient second pulse, when the SSC and SAR peak simultaneously. TDS_{sil} and TDS_{carb} contribute 39.5±15.2% and 27.5±16.7%, respectively (Fig. 3c).

Enriched ratios of less than ~~1~~ one indicate dilution, and values greater than ~~1~~ one indicate concentration. Since we set the ion concentration of rainfall to be constant during the typhoon event, the enriched ratio of precipitation is constant throughout the observation period. At Nanxiong Bridge, the evaporites enriched ratio increases from 0.4 to 1.7 between the two pulses and decreases to 0.1 at the discharge peak. The silicates enriched ratio increases from 1 to 1.5 before the first pulse and decreases to 0.1 at the peak of discharge, then returns to 1 before the observation ends. The concentration attributed to carbonates is always diluted. The evaporites and carbonates enriched ratio ~~have~~ has a statistically significant negative correlation with discharge (evaporites: ρ = -0.67, carbonates: -0.60, p<0.05) and the silicate enriched ratio has a negative correlation with discharge (ρ = -0.32), indicating dilution by typhoon rainfall (Fig. 3d). At Guting Bridge, the evaporites enriched ratio has two peaks during the two pulses with a value of 5.2 at the first peak, a value of 4.7 at the second peak. After the event, the value returns to about 1.2. Notably, the evaporites enriched ratios during ~~the~~ both pulses are similar, but the peak discharge of the second pulse is 5.5 times higher than that of the first pulse. The silicate

276 enriched ratio has an analogous pattern with the evaporites enriched ratio, but the enriched ratio is

277 smaller. Similar to Nanxiong Bridge, the carbonates enriched ratio is always diluted at Guting Bridge

278 (Fig. 3e). The evaporite and silicate enriched ratio shows a statistically significant positive correlation

279 ($\rho = 0.96$, $p<0.05$), and the evaporite and silicate enriched ratios have a statistically significant positive

280 correlation with SAR ($\rho = 0.86$, $\rho = 0.84$, $p<0.05$). We also use the concentration–discharge (cQ)

281 relationship of each ion at rising and recession limb, as well as baseflow at Nanxiong Bridge to assess

282 the state of dilution behavior (Fig. S2). Overall, our results show that all ions are in a dilution, and the

283 dilution in recession limb is stronger than that in rising limb, except for SO_4 during baseflow ($\theta=0.07$).

284 The concentration of Na, Cl and K during baseflow have a higher variability than the values during

285 the event. Additionally, Na, Cl, and SO_4 increase the concentration with increasing flow at the certain

286 period of rising limb.

288
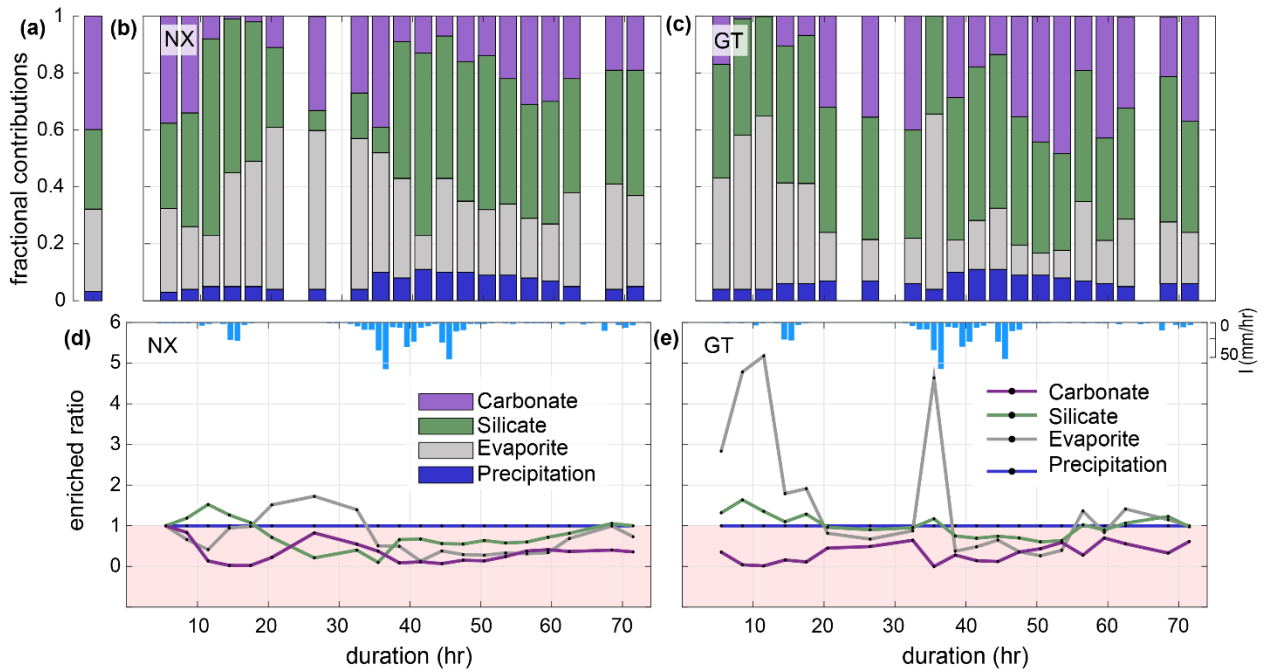
Figure 3. Timeseries illustrating TDS sources during the typhoon event at the two sampling sites. Fig.3a shows the average proportion of TDS for the non-typhoon period from September 2014 to December 2016 at Nanxiong Bridge; Fig.3b-c denotes the endmember contributions to TDS at Nanxiong Bridge dataset and Guting Bridge dataset from the typhoon period; the purple bar denotes TDS_{carb} (Eq. 8); green denotes TDS_{sil} (Eq. 7); the gray bar denotes $TDS_{evaporite}$ (Eq. 6); the blue bar denotes TDS_{rain} (Eq. 4). Fig.3d-e denotes the enriched ratio of ion concentrations by TDS sources from the Nanxiong Bridge dataset and Guting Bridge dataset during the typhoon period. The purple line denotes TDS_{carb}, the green line denotes TDS_{sil}, the gray line denotes $TDS_{evaporite}$, the blue line denotes the TDS_{rain}, and blue bar denotes hourly precipitation (I) at GTK station.

4.2 Evaporite, silicate and carbonate dissolution over time

We calculated the enriched ratios of ions (i.e., Na^+, Cl^-, Ca^{2+} and SO_4^{2-}) that are sourced from evaporites (i.e., halite ($NaCl$) and gypsum ($CaSO_4$)). The variability in the concentrations of each of these ions reflects the overall trends in TDS (Fig. 3d-e & Fig. 4).

At Nanxiong Bridge, all evaporite and carbonate ions have a statistically significant negative correlation with discharge. The enriched ratios in evaporite Na^+, Cl^- and SO_4^{2-} have the same trend (Fig. 4), which show an initial decrease during the first pulse, followed by an increase to 2 between the two pulses, and a final decrease during the second pulse. Evaporite Ca^{2+} shows a similar trend with evaporite Na^+, Cl^- and SO_4^{2-}, but the values are below 1. The enriched ratios of silicate Na^+, Ca^{2+}, ~~and~~ ~~SO_4^{2-}~~ show an increase during the first pulse and a decrease to less than 1 before the rainfall peak, followed by an increase from about 0.06 to 1.11 at the end of observation. At Guting Bridge, all evaporite ions have a statistically significant positive correlation with the corresponding silicate ions (Na^+, $\rho = 0.98$; Ca^+, $\rho = 0.81$~~; $SO_4^{2-}=0.98$~~, $p<0.05$). Evaporite Na^+, Cl^-, and SO_4^{2-} each have two peaks that occur prior to the maximum rainfall and reflect a factor of 5 increase in the enriched ratio. Compared with Nanxiong Bridge (downstream), the enriched ratio in evaporite Ca^{2+} at Guting Bridge concentrates at the onset of the first pulse and after peak discharge. Additionally, the enriched ratios of carbonate at Guting Bridge are similar to Nanxiong Bridge, and are always below 1.
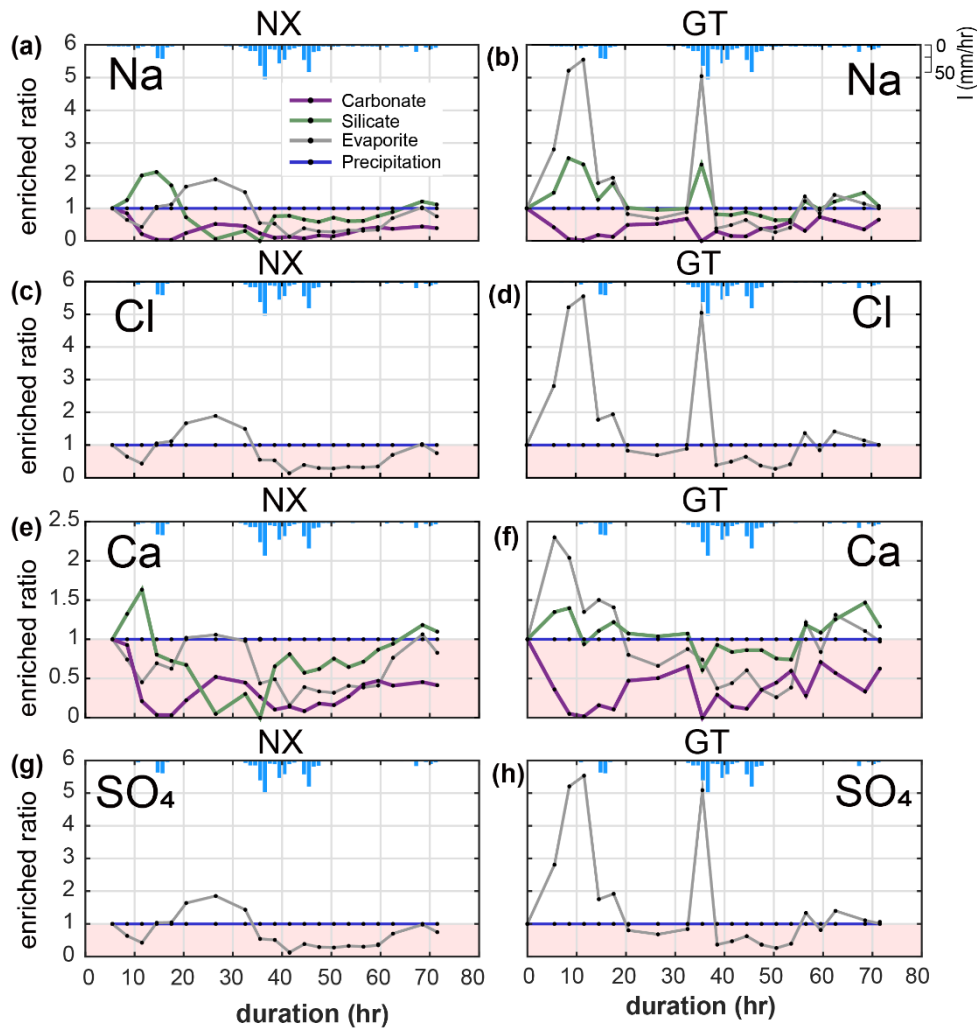
Figure 4. Time-series patterns in enriched ratio at two sampling sites. NX denotes the Nanxiong Bridge dataset and GT denotes Guting Bridge dataset. The pink area indicates enriched values below 1. Blue bar denotes hourly precipitation (I) at Gutingkeng station.

Gaillardet et al. (1999) documented that dissolved ions ratios of Ca/Sr and Na/Sr are distinct for carbonates (low Na/Sr, high Ca/Na) versus silicates or evaporites (high Na/Sr, low Ca/Na). We use these ratios to elucidate potential mixing between carbonates, ~~and~~ silicates~~/~~, and evaporite endmenbers~~s~~ (Fig. 5). At Nanxiong Bridge, non-typhoon ratios of Na/(1000*Sr) and Ca/(1000*Sr) are 0.23–0.68 and 0.19–0.35, respectively (Table S4). These values increase markedly during the typhoon events, with enriched ratios of Na^+ exceeding 5 at T = 11.5 and 35.5 hr. The high concentration of Na^+, Cl^- and SO_4^{2-} (as illustrated in the enriched ratio) indicate that there is enhanced dissolution of evaporites at the onset of the typhoon event, especially at Guting Bridge. Subsequently, the

329   concentration of Na$^+$ decreased with sustained rainfall. Then, the ratios approach the

330   silicates/carbonates weathering (high Na/Sr, high Ca/Sr ratios) after the peak discharge.

331
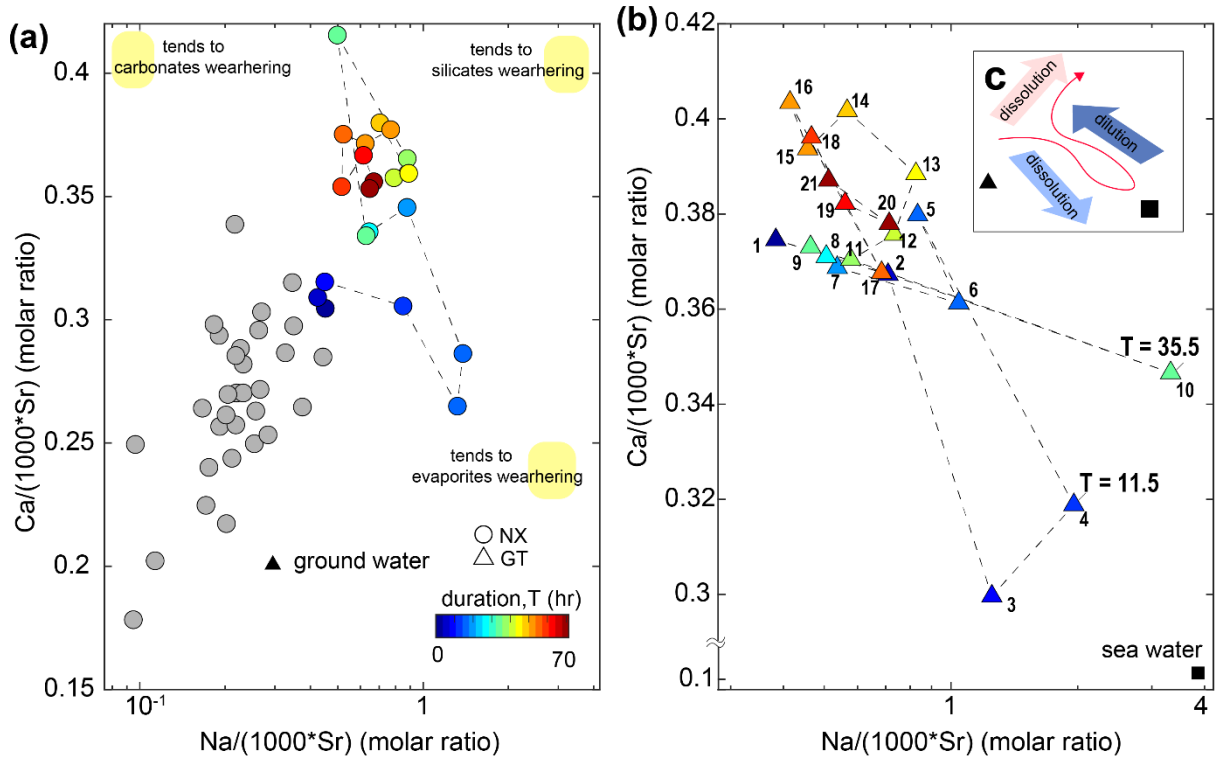
333   **Figure 5.** Molar ratio mixing diagrams of Erren River waters for (a-b) Na/(1000*Sr) versus
334   Ca/(1000*Sr), circles denote dataset at Nanxiong Bridge, and triangles denote dataset at Guting Bridge.
335   Colorbar denotes survey duration. Gray circles denote the dataset at Nanxiong Bridge during baseflow
336   conditions from 2014 to 2016. The black triangle illustrates the groundwater endmember (Chao et al.,
337   2011); the black square illustrates the seawater endmember. Numbers in the triangle represent the time
338   sequence, 1 represents the start point, and 21 represents the end point. Yellow areas indicate trends in
339   weathering types rather than the locations of endmember. (c) Illustration of dynamic weathering. The
340   red line indicates the direction of change with time. The light blue arrow denotes dissolution of
341   evaporite, the dark blue arrow denotes dilution from rainfall, and the red arrow denotes dissolution of
342   suspended sediment.

343

344   **5. Discussion**

345   **5.1 Relationships between dissolved evaporite and river water chemistry**

346   Before the survey, the monthly rainfall of the study area was 72.5 mm, which is only 18% of the

average monthly rainfall, implying that it provides a relatively dry environment for accumulating evaporites on the slope surface. Under maximum rainfall intensity, Na^+, Cl^- and SO_4^{2+} at Guting Bridge show markedly increased concentrations at the onset of the typhoon, peaks in enriched ratios that exceed 5 (Fig. 4), and the greatest contribution of dissolved ions from evaporites (Fig. 3). ~~In addition,~~ Calculated with pore water chemistry during the dry season from the same study site, the sodium absorptions ratio (SAR) is 240.8 and exceeds the threshold value of 13. During the typhoon event, the river water SAR has a maximum value of 4.41 at Guting Bridge (3.14 at Nanxiong Bridge), suggesting soil deflocculation within river is weaker than on the hillslopes. However, the ~~sodium absorptions ratio (SAR)~~ has a statistically significant positive correlation with $TDS_{evaporite}$ ($\rho = 0.86$, p<0.05) at Guteng Bridge (upstream). ~~During the typhoon event, the SAR increases from 4.8 to 24.9 and exceeds the threshold value of 13 at the incipient first pulse and at the incipient second pulse.~~ This pattern indicates that excess sodium is effective at inducing material dispersion at hillslopes and thus, contributing to a higher suspended sediment load. The trend of river water SAR is able to reflect the extent of dissolved Na^+ from hillslope. (Fig. 2).

These observations and results suggest that rainwater in the typhoon event rapidly dissolves the evaporites on the slope surface, which produces high measured concentrations of Na^+, Cl^-, and SO_4^{2+} during the time of peak precipitation (30-40 hr of duration). Furthermore, the dissolution of the near-surface evaporite deposits should be most heavily influenced by runoff from the hillslopes, so we expect that excess sodium and enhanced erosion will be most significant on the hillslopes.

At Nanxiong Bridge, we observe a 10-hour delay in the peak enriched ratio relative to the SAR (Fig. 3d) and overall lower enriched ratios relative to Guteng Bridge (Fig. 3d-e). We suggest that dilution and the transport distance from the badlands ~~is~~ are responsible for this. The two catchments have a similar areal extent of badlands within the total catchment area, which is about 2.49% at Nanxiong Bridge catchment and 2.37 % in Guting Bridge catchment. Badlands contribute considerable evaporite

solutes (Chou, 2008), but the higher downstream drainage area will result in dilution of the solutes without additional inputs. Additionally, Nakata and Chigira (2009) have observed that salt dissolution induces an increase in electrical conductivity during intermittent rainfall events and decreases gradually after rainfall events when evaporation and salt precipitate. Therefore, re-crystalization during the transportation is to be expected.

5.2 From evaporite dissolution to silicate weathering

Our observations show that silicate weathering during the typhoon event contributes 16.8 ton/km^2/yr~~the water chemistry of the typhoon event is dominated by silicate weathering at 16.8 ton/km^2/day~~, corresponding to~~contributing~~ 16.6% ~~to~~ of the annual silicate weathering flux (Table S3). Additionally, we observed a change in dominant chemical weathering mechanism during the typhoon event. We rule out significant contributions from groundwater and deep seawater after peak discharge, since ratios shift to higher Na/Sr, and Ca/Sr ratios relative to the non-typhoon ratio (Fig. 5a–b), and the Ca/Sr ratio of mud volcanoes in the study site is one order of magnitude less than river water (Chao et al., 2011). Carbonate weathering is the primary contributor of Ca^{2+} for most of the world's large rivers (Gaillardet et al. 1999), but the increased Na^+ and consistently enriched ratio of carbonate Ca^{2+} does not make this a likely main contributor to the Erren River during the typhoon. We thus suggest that the primary contributor to weathering is ~~from~~ enhanced silicate dissolution. This interpretation is supported by the temporal evolution of the enriched ratio of silicate Ca^{2+}, which gradually increases after the discharge peak, to approach a value of about 1 at the end of survey (Fig. 4e&f). As such, in the waning of the event, excess Ca^{2+} originates from a silicate source. Therefore, we suggest that the ratios shift to higher Na/Sr, Ca/Sr ratios ~~is~~ due to enhanced silicate weathering during the typhoon. We also observe that the masses of Na and Ca are reduced by 10.6% and 9.9%, respectively, in the suspended sediment during the course of the typhoon event (Table S6).~~—~~

398 Given that the sediment transported in the channel is supplied by physical erosion, we suggest that

399 physical erosion in our study site enhances silicate chemical weathering, which is consistent with

400 previous studies (Chung, 2002; Chou, 2008). ~~Thus~~Moreover, we associate the change in weathering

401 regime during the course of the typhoon with abrasive erosion of silicate sediments in the channel.

402 Mechano-chemical dissolution of weakly bound ions, e.g., F^- from the fresh muscovite surfaces is

403 driven by abrasion under high energy sediment transport with reorganization of the river bed

404 (Andermann et al., 2022). Mudstone~~s~~ ~~is~~are mainly composed of silicate minerals (e.g., illite and

405 chlorite minerals) (Tsai, 1984a), and a few swelling clay minerals (e.g., montmorillonite), which

406 provide an abundant silicate pool. We suggest that high suspended sediment concentrations, combined

407 with high energy flow during the typhoon, caused increased silicate input from the weathered silicates

408 in the suspended sediment. This trend can explain about 10% of the reduced mass and it has also been

409 observed ~~on~~ in typhoon-driven silicate chemical weathering from silicate minerals at surface (Meyer

410 et. al., 2017). Importantly, the global annual silicate weathering flux of rivers is 15.7 ton/km^2/yr

411 (Gaillardet et al. 1999), relative to our value of 16.8 ton/km^2/yr.~~the silicate weathering flux that we~~

412 ~~calculate in this study is comparable to the global annual flux of rivers (Gaillardet et al. 1999)~~,

413 suggesting that individual stochastic events may have global relevance.

414

415 **5.3 Typhoon-controlled cycles of physical and chemical erosion**

416 Evaporites, including halite (NaCl) and gypsum (CaSO$_4$), are found in few sedimentary environments,

417 and they are often excluded from the estimation of CO_2 consumption ~~global chemical weathering~~

418 ~~cycles~~ (Gaillardet et al., 1999). Compared to silicate rocks, the relation between evaporites weathering

419 and physical erosion has rarely been discussed. Through the interactions among riverine chemistry,

420 suspended sediment properties, and previous soil water chemistry studies, we suggest a positive

421 feedback cycle of physical-chemical erosion driven by mobile dissolved evaporite (Fig. 5). The

422 feedback cycle includes three steps. (1) precipitation and deposition of evaporite during the dry season

423 in near-surface mudstone desiccation cracks through capillary transport (Higuchi et al., 2013, 2015;

424   Nakata and Chigira, 2009). In the dry season, exposed bedrock with low water content develops

425   desiccation cracks (Allen, 1982; Goehring et al., 2010; Kindle, 1917; Seghir and Arscott, 2015; Xiaa

426   and Hutchinson, 2000), providing space for the re-precipitation of evaporite minerals. Using evidence

427   from core samples in mudstone bedrock at the study site, the depth of the crack of about 20 cm can be

428   regarded as the thickness of the weathering layer. Higuchi et al. (2013) suggested that the weathering

429   layer in the top 10 cm of mudstone can easily be eroded by intense rainfall. Erosion exposes fresh

430   bedrock, which would dry in the following dry season and further produce weatherable material.

431

432   (2) Rainfall dissolves the evaporites, producing sodic water that increases physical erosion during

433   typhoon events. The resulting dissolved sodium causes higher hillslope erosion by deflocculation,

434   leading to increased suspended sediment in the channels. In the study site, hillslope erosion rate is

435   about 9-30 cm/year (Higuchi et al., 2013; Yang et al., 2021a). At Nanxiong Bridge, the denudation rate

436   approaches about 142,857 ton/km^2/yr, measured from river suspended load (Dadson et. al., 2003), and

437   the chemical weathering flux is 124-235̶7 ton/km^2/yr (Chou, 2008; this study). The high hillslope

438   erosion rate ensures a steady supply of freshly exposed bedrock, allowing for high chemical weathering

439   rates.

440

441   (3) Physical erosion enhances silicate weathering and bedrock exposure on hillslopes. Clay minerals

442   in mudstone deposits are abraded from the abundantly available sediment and provide material for

443   silicate weathering in streams. Ultimately, with frequent typhoon events and high temperatures in the

444   study area, this dynamic cycle could repeat several times a year.

445
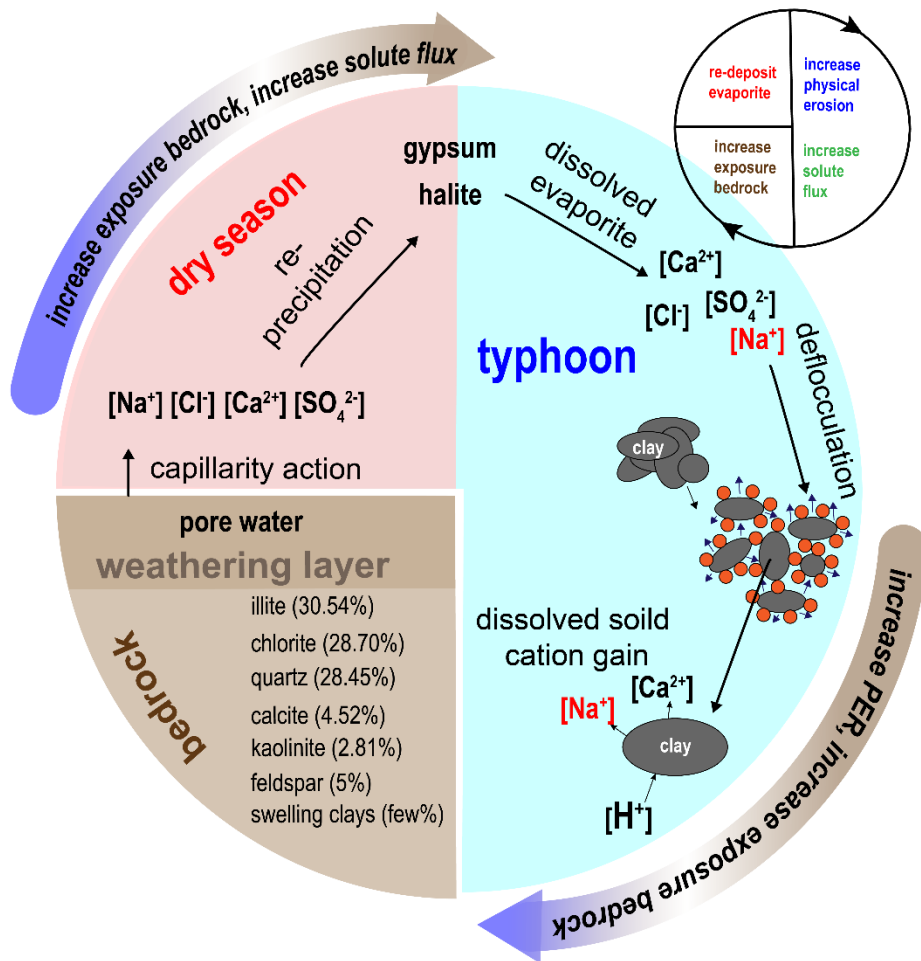
Figure. 6. Cycle of feedback between physical erosion rate (PER) and solute flux ~~chemical weathering rate (CWR)~~ in badlands catchment. Red blocks represent dry season conditions. Blue region represents typhoon conditions. Brown region represents the bedrock and indicates the type and proportion of minerals of mudstone (Tsai, 1984b).

450

6. Conclusion

We presented major element compositions of stream water from two sites in the Erren River catchment at three-hour intervals during a three-day typhoon event in 2017. At ~~the~~ Guteng Station (upstream), $TDS_{evaporite}$ is covariant with TDS_{sil}, the sodium adsorption ratio, and the suspended sediment concentration, which can be assigned to dissolved evaporite (e.g., halite and gypsum). The excess sodium in the evaporite deposits causes material dispersion through deflocculation, which enhances the suspended sediment flux. Our observations show that the water chemistry of the typhoon event is ~~dominated~~ mainly contributed by silicate weathering at 16.8 ton/km^2/yr~~day~~ and evaporite weathering

at 10.9 ton/km^2/yr, in contrast with baseflow (non-typhoon) conditions that are mainly contributeddominated by carbonate weathering. Moreover, during the course of the typhoon, we observed a shift from predominantly evaporite weathering during peak precipitation to silicate weathering at peak discharge.

Combining the observation of riverine chemistry, suspended sediment properties, and previous soil water chemistry studies, we propose a feedback cycle between physical erosion and chemical weathering in badlands topography, illustrating that precipitation of evaporites during the dry season produces sodic water during typhoon events and preferentially triggers higher local erosion. The enhanced hillslope erosion and abrasive effects of clay in a high discharge stream enhance bedrock exposure on hillslopes and silicate weathering, respectively. Newly exposed bedrock then produces more weathered material. Although measurements of bedrock mineral chemistry and Sr isotope are still needed for confirming sources of excess sodium and calcium (Fig. 5), we suggest that the conceptual model could provide an insight into landscape change of badlands. The results from our study suggest that high erosion rates in mudstone badlands of the Erren River catchment is are due to both weakened lithology and to the interaction between evaporites and hillslope erosion.

Data availability. Relevant data supporting the findings of the study are available in the Supplementary Information, or from the corresponding author upon request. Source data are provided with this paper.

Author contributions. C.-J.Y. designed the study and conducted field surveys, data analysis, and modelling. P.-H. C. conducted data analysis. S. X. conducted modelling. T. Y. T. provided the verified data. J.-C.L. and J.-C. Huang contributed to the scientific discussion, interpretation, and paper preparation.C.-J.Y., E. D. E. and J.M.T. wrote the paper with input of all authors. S. X. conducted modelling. T. Y. T. provided the verified data. J. C.L. and J. C. Huang contributed to the scientific discussion, interpretation, and paper preparation.

Competing interests. The authors declare that they have no competing interests.

Acknowledgements. We express our gratitude to Niels Hovius for fruitful discussions that greatly improved this work. Special thanks are also given to Sheng-Wei Guo, Meng-Chang Lu for field work. This is study was supported by grants from National Science and Technology Council, Taiwan to Ci-Jian Yang (MOST 110-2917-I-564-009-).

References

1.   Allen, J.R.L.: Sedimentary structures: Their Character and Physical Basis. Developments in sedimentology. 30B, II. Elsevier, Amsterdam. 1982.

2.   Andermann, C., Galy, A., Hennig, S., Zimmermann, B., Tipper, E. T., Erlanger, E., Cook, K. L., Schleicher, A., Benning, L., and Hovius, N.: Erosion and weathering forensics of a catastrophic glacial lake outburst flood in Nepal, EGU General Assembly 2022, Vienna, Austria, 23–27 May 2022, EGU22-10417, https://doi.org/10.5194/egusphere-egu22-10417, 2022.

1.3.   Ayers, R., Westcot, D.: Water quality for agriculture. FAO Irrigation and drainage paper 29, 1985.

2.4. Burke, A., Present, T., Paris, G. Rae, Emily C.M., Sandilands, B. Gaillarde, J., Peucker-Ehrenbrink, B., Fischer, W. W., McClelland, J. W., Spencer, R. G. M., Voss, B. M., Adkins, J. F.: Sulfur isotopes in rivers: Insights into global weathering budgets, pyrite oxidation, and the modern sulfur cycle. Earth and Planetary Science Letters, 496. https://doi.org/10.1016/j.epsl.2018.05.022https://doi.org/10.1016/j.epsl.2018.05.022ff.ffhal-02118784, 2018

3.5.   Calmels, D., Galy, A., Hovius, N., Bickle, M. J., West, A. J., Chen, M.-C., Chapman, H.: Contribution of deep groundwater to the weathering budget in a rapidly eroding mountain belt, Taiwan. Earth and Planetary Science Letters, 303 (1-2), 48–58.

511   https://doi.org/10.1016/j.epsl.2010.12.032, 2011

512   4.6. Carey, A. E., Gardner, C. B., Goldsmith, S. T., Lyons, W. B., Hicks, D. M.: Organic carbon

513   yields from small, mountainous rivers, New Zealand. Geophysical Research Letters, 32, 15404.

514   https://doi.org/0.1029/2005GL023159, 2005.

515   5.7.Chao, H.-C., You, C.-F., Wang, B.-S., Chung, C.-H., Huang, K.-F.: Boron isotopic composition of

516   mud volcano fluids: Implications for fluid migration in shallow subduction zones. Earth and

517   Planetary Science Letters, 305. https://doi.org/10.1016/j.epsl.2011.02.033, 2011.

518   6.8. Cheng, Y.-C., Yang, C.-J., Lin, J.-C.: Application for Terrestrial LiDAR on Mudstone Erosion

519   Caused by Typhoons. Remote sensing, 11(20), 2425. https://doi.org/10.3390/rs11202425, 2019.

520   7.9. Chou, C.-L.: Sediment Weathering and River Water Chemistry in the Erren Drainage Basin,

521   Southern Taiwan. Master thesis of Department of Earth Sciences, National Cheng Kung

522   University, 1–103, 2008.

523   8.10.Chung, S.-L.: Preliminary Geochemical and Isotopes study of the Erren river water. Master

524   thesis of Department of Earth Sciences, National Cheng Kung University, 1–95, 2002.

525   9.11.Clift, P. D., Wan, S., Blusztajn, J.: Reconstructing chemical weathering, physical erosion and

526   monsoon intensity since 25Ma in the northern South China Sea: A review of competing proxies.

527   Earth-Science Reviews, 130, 86–102. https://doi.org/10.1016/j.earscirev.2014.01.002, 2014.

528   10.12. Dadson, S. J., Hovius, N., Chen, H., Dade, W. B., Hsieh, M.-L., Willett, S. D., Hu, J.-C.,

529   Horng, M.-J., Chen, M.-C., Stark, C. P., Lague, D. Lin, J.-C.: Links between erosion, runoff

530   variability and seismicity in the Taiwan orogen. Nature, 426(6967), 648–651,

531   https://doi.org/10.1038/nature02150, 2003.

532   11.13. Emberson, R., Hovius, N., Galy, A., Marc, O.: Chemical weathering in active mountain

533   belts controlled by stochastic bedrock landsliding. Nature Geoscience, 9, 42–47.

534   https://doi.org/10.1038/ngeo2600, 2016.

535   12.14. Faulkner, H., Alexander, R., Teeuw, R., Zukowskyj, P.: Variations in soil dispersivity

536   across a gully head displaying shallow sub-surface pipes, and the role of shallow pipes in rill

initiation. Earth Surface Process and Landforms. 29, 1143–1160.

https://doi.org/10.1002/esp.1109, 2004.

13.15.   Gaillardet, J., Dupre, B., Louvat, P., Allegre, C. J.: Global silicate weathering and CO_2

consumption rates deduced from the chemistry of large rivers. Chemical Geology, 159, 3–30.

https://doi.org/10.1016/S0009-2541(99)00031-5, 1999.

14.16.   Goehring, L., Conroy, R., Akhter, A., Cleggb, W.J., Routh, A.F.: Evolution of mud-crack

patterns during repeated drying cycles. Soft Matter, 6, 3562–3567.

https://doi.org/10.1039/B922206E, 2010.

17. Hanson, B., Grattan, SR., Fulton, A.: Agricultural salinity and drainage. University of California

Irrigation Program, Davis., 1999.

15.18.   Hartshorn, K., Hovius, N., Dade, W. B. Slingerland, R. L.: Climate-Driven Bedrock

Incision in an Active Mountain Belt. Science, 297, 2036–2038. https://10.1126/science.1075078,

2002.

16.19.   Higuchi, K., Chigira, M., Lee, D.-H.: High rates of erosion and rapid weathering in a Plio-

Pleistocene mudstone badland, Taiwan. Catena, 106, 68–82.

https://doi.org/10.1016/j.catena.2012.11.005, 2013.

17.20.   Higuchi, K., Chigira, M., Lee, D-H., Wu, J-H.: Rapid weathering and erosion of mudstone

induced by saltwater migration near a slope surface. Journal of Hydrologic Engineering, 20(6),

C6014004. https://doi.org/10.1061/(ASCE)HE.1943-5584.0001105, 2015.

21. Horneck, D.S., Ellsworth, J.W., Hopkins, B.G., Sullivan, D.M., Stevens, R.G.: Managing Salt-

Affected Soils for Crop Production. PNW 601-E. Oregon State University, University of Idaho,

Washington State University, 2007.

18.22.   Huang, J.C., Lee, T.Y., Kao, S.J., Hsu, S.C., Lin, H.J., Peng, T.R.: Land use effect and

hydrological control on nitrate yield in subtropical mountainous watersheds. Hydrology and

Earth System Science, 16(3), 699-714. https://doi.org/10.5194/hess-16-699-2012, 2012.

19.23.   Kemeny, P. C., Torres, M. A.: Presentation and applications of mixing elements and

dissolved isotopes in rivers (MEANDIR), a customizable MATLAB model for Monte Carlo inversion of dissolved river chemistry. American Journal of Science, 321(5), 579–642. https://doi.org/10.2475/05.2021.03, 2021.

24. Kindle, E.M.: Some factors affecting the development of mud-cracks. The Journal of Geology, 25(2), 135–144. https://doi.org/10.1086/622446, 1917.

20.25. Knapp, J. L., von Freyberg, J., Studer, B., Kiewiet, L., & Kirchner, J. W.: Concentration–discharge relationships vary among hydrological events, reflecting differences in event characteristics. Hydrology and Earth System Sciences, 24(5), 2561-2576. https://doi.org/10.5194/hess-24-2561-2020, 2020.

21.26. Lee, D.-H., Lin, H.-M., Wu, J.-H.: The basic properties of mudstone slopes in southwestern Taiwan. Journal of GeoEngineering, 2(3), 81–95. https://doi.org/10.6310/jog.2007.2(3).1, 2007.

22.27. Lee, Y.-J., Chen, P.-H., Lee, T.-Y., Shih, Y.-T., Huang, J.-C.: Temporal variation of chemical weathering rate, source shifting and relationship with physical erosion in small mountainous rivers, Taiwan, Catena, 190. https://doi.org/10.1016/j.catena.2020.104516, 2020.

23.28. Lu, S.-C. and Lin, N.-H.: Monitoring and component analysis of acid rain research project. Environmental Protection Agency, Taiwan, 2014.

24.29. Lyons, W. B., Carey, A. E., Hicks, D. M., Nezat, C. A.: Chemical weathering in high-sediment-yielding watersheds, New Zealand. Journal of Geophysical Research-Earth Surface, 110, 11. https://doi.org/10.1029/2003JF000088, 2005.

25.30. Maher, K., and Chamberiain, C. P.: Hydrological Regulation of Chemical Weathering and the Geologic Carbon Cycle. Science, 343, 1502–1504. https://doi.org/10.1126/science.1250770, 2014.

26.31. Meyer, K. J., Carey, A. E., You, C.-F.: Typhoon impacts on chemical weathering source provenance of a High Standing Island watershed, Taiwan. Geochimica et Cosmochimica Acta, 215, 404–420. https://doi.org/10.1016/j.gca.2017.07.015, 2017.

27.32. Mitchell, J. K.: Volume change behavior. In: Mitchell, J.K., Soga, K. (Eds.), Fundamentals

of Soil Behavior. Wiley, 293–333, 1993.

28.33.	Moon, S., Huh, Y., Qin, J.H., van Pho, N.: Chemical weathering in the Hong (Red) River basin: Rates of silicate weathering and their controlling factors. Geochimica et Cosmochimica Acta, 71, 1411–1430. https://doi.org/10.1016/j.gca.2006.12.004, 2007.

29.34.	Nadler, A., Levy, G. J., Keren, R., Eisenberg, H.: Sodic Calcareous Soil Reclamation as Affected by Water Chemical Composition and Flow Rate. Soil Science Society of America Journal. 60 (1): 252. Bibcode:1996SSASJ.60.252N. https://doi:10.2136/sssaj1996.03615995006000010038x, 1996.

30.35.	Nakata, E., Chigira, M.: Geochemistry of erosion processes on badland slopes. A case study of the Gutingkeng formation where mud volcanoes are distributed in southern Taiwan. Journal of Geography, 118(3), 511–532, 2009.

31.36.	Negrel, P., Allegre, C.J., Dupre, B., Lewin, E.: Erosion sources determined by inversion of major and trace element ratios and strontium isotopic ratios in river water: The Congo Basin case. Earth and Planetary Science Letters, 120, 59–76. https://doi.org/10.1016/0012-821X(93)90023-3, 1993.

32.37.	Rengasamy, P., Greene, R.S.B., Ford, G.W., Mehanni, A.H.: Identification of dispersive behavior and the management of red-brown earths. Australian Journal of Soil Research, 22, 413–443. https://doi.org/10.1071/SR9840413, 1984.

33.38.	Rengasamy, P., Olsson, K. A.: Sodicity and soil structure. *Australian Journal of Soil Research*, 29, 935–952. https://doi.org/10.1071/SR9910935, 1991.

34.39.	Seelig, B. D.: Salinity and Sodicity in North Dakota Soils. EB-57. North Dakota State University, Fargo, ND, 2000.

35.40.	Seghir, R., Arscott, S.: Controlled mud-crack patterning and self-organized cracking of polydimeth. Scientific Report, 5, 14787. https://doi.org/10.1038/srep14787, 2015.

36.41.	Sherard, J. L., Dunnigan, L. P., Decker, R. S., Steele, E. F.: Identification and nature of dispersive soils. Journal of the Geotechnical Engineering Division, 102, 287–301. 1976.

616   ~~37.~~42.   Tsai, J. S.: The study on basic properties of mudstone and stabilization methods for

617   mudstone cut slope in southwestern Taiwan. Master Thesis of Civil Engineering Department,

618   National Cheng Kung University, Tainan, Taiwan, 1984b.

619   ~~38.~~43.   Xia, Z. C., Hutchinson, J. W.: Crack patterns in thin flms. Journal of the Mechanics and

620   Physics of Solids, 48, 1107–1131. https://doi.org/10.1016/S0022-5096(99)00081-2, 2000.

621   ~~39.~~44.   Yang, C.-J., Turowski, J. M. Hovius, N., Lin, J.-C., Chang. K.-J.: Badland landscape

622   response to individual geomorphic events. Nature Communications, 12(1):4631.

623   https://doi.org/10.1038/s41467-021-24903-1, 2021a.

624   ~~40.~~45.   Yang, C.-J., Jen, C.-H., Cheng, Y.-C., Lin, J.-C.: Quantification of mudcracks-driven

625   erosion using terrestrial laser scanning in laboratory runoff experiment. Geomorphology, 375.

626   https://doi.org/10.1016/j.geomorph.2020.107527, 2021b.

627   ~~41.~~46.   Yang, C.-J., Yeh, L.-W., Cheng, Y.-C., Jen, C.-H., Lin, J.-C.: Badland Erosion and Its

628   Morphometric Features in the Tropical Monsoon Area. Remote sensing, 11(24), 3051.

629   https://doi.org/10.3390/rs11243051, 2019.